LASER INTERFEROMETER GRAVITATIONAL WAVE OBSERVATORY

- LIGO -

CALIFORNIA INSTITUTE OF TECHNOLOGY

MASSACHUSETTS INSTITUTE OF TECHNOLOGY

Document Type	**LIGO-T010119-00-D**	Oct. 16th, 2001

The Characterization and Modeling of the Length Sensing and Control (LSC) Subsystem

Luca Matone

Distribution of this draft:
TBD

This is an internal working note
of the LIGO Project.

California Institute of Technology
LIGO Project - MS 18-34
Pasadena, CA 91125
Phone (626) 395-2129
Fax (626) 304-9834
E-mail: info@ligo.caltech.edu

Massachusetts Institute of Technology
LIGO Project - MS 20B-145
Cambridge, MA 01239
Phone (617) 253-4824
Fax (617) 253-7014
E-mail: info@ligo.mit.edu

WWW:http//www.ligo.caltech.edu/

Contents

1 Introduction

The goal of the Length Sensing and Control (LSC) Subsystem is to maintain optical resonance in the interferometer such that a linear signal, proportional to the metric strain, is available at the readout. The description of the as-designed system can be found in [1].

In the present document, the first results of the LSC characterization and modeling effort are given, focusing on the electronic, mechanical and optical transfer functions (TF) of the 2 km interferometer (IFO) at Hanford (LHO). Based on the gathered information, a model will be created, using LIGO's simulation engine e2e[2], to generate and compare the

- frequency response to gravitational wave (GW) excitation;
- strain sensitivity;

with the observed ones.

NOTE: the present work is far from complete and will be periodically updated. However, a good portion of the LSC frequency response has been characterized and modeled with Matlab, and the results are given. A brief overview of the system is also presented.

2 The LSC Subsystem

Currently, only part of the final control topology is in place on site: the IFOs (2k at LHO and 4k at LLO) have been locked to the laser. This will not be exactly the case once the complete Common Mode servo will be in place. For the first five engineering runs, however, the four degrees of freedom (DOF) Δl_-, Δl_+, ΔL_- and ΔL_+ have been controlled using the Large Optic Suspension (LOS) actuators.

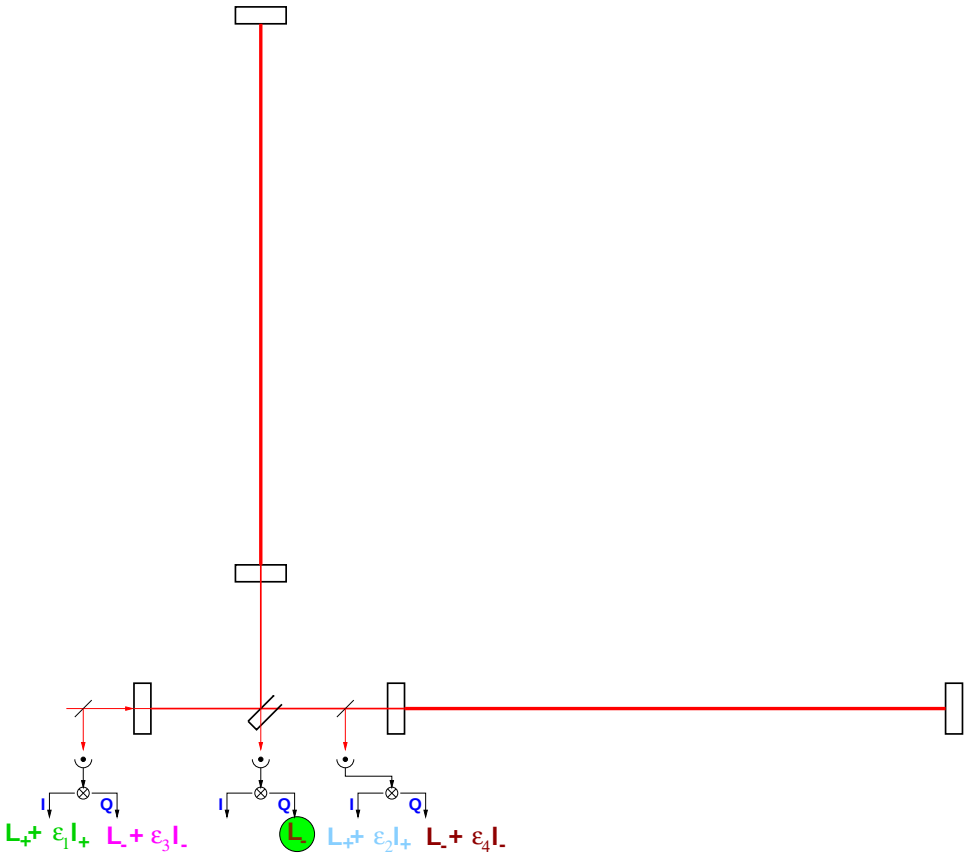

Figure 1: The IFO's output ports and their dependence on the four DOFs.

How does the LSC subsystem detect any changes in the four DOFs, and what kind of signal processing and actuation is necessary to maintain the IFO in operation? These issues are addressed by the LSC and a brief description will be given in the sections to come (see [1, 3, 4, 5, 6] for a complete overview).

2.1 Extracting Δl_-, Δl_+, ΔL_- and ΔL_+

The sensing of the four DOF has been extensively addressed in the past. The detection scheme, referred to as the Pound-Drever-Hall reflection locking technique[7], consists in phase modulating the input laser beam with a resonant Pockels cell at an RF frequency. This frequency is chosen such that the sidebands resonate, with the carrier, in the recycling cavity but are non-resonant in the arms. By demodulating the RF signal from the photodiode (PD) monitoring the IFO output beam, two signals are generated, referred to as the inphase (I) and quadrature (Q) components. These (error) signals, around IFO's operation point, are linear with respect to the four DOFs.

The following output beams, shown in Fig.(1), are monitored:

- the beam reflected from the recycling mirror (REFL);
- the beam at the interference port (ASY);

- and the beam reflected off of the pickoff mirror placed in the recycling cavity after the beam splitter (POY).

Fig.(1) also shows the dependence of the six error signals with the four DOFs.

3 Interferometer Control

The detection scheme produces a set of error signals proportional to the four DOFs. These signals need to be amplified, filtered, and applied to the actuators in order to keep the IFO in operation. As previously mentioned, the actuators that will be addressed are the LOS controllers. The signal flow, from the PD to the controllers, is shown in the diagram of Fig.(2) and consist of

- the output PD, converting the laser beam to an RF signal which is then demodulated to give two error signals (I and Q);
- the Whitening filter whose goal is to match the excursion of the error signal to the input range of the ADC;
- the Anti-Aliasing filter, which low passes the Whitening output;
- the ADC which digitizes the output of the Anti-Aliasing filter. Once digitized, three filter banks are applied to
  - invert the Whitening process;
  - run the IFO in different configuration;
  - whitening again the signal to match its excursion to the DAC;
- the Anti-Imaging filter, which low-passes the DAC output;
- the De-Whitening filter, whose goal is to invert the digital whitening process.

4 The Characterization of the Electronics: Filtering

The filtering properties of the electronics have been recently measured and the results are given.

4.1 The Whitening Board (D990694)

Fig.(3) shows the TF measurement between output and input of the Whitening board with the filtering enabled. The upper two graphs of Fig.(3) show the magnitude and phase of the TF, whereas the bottom two graphs show the deviation of the TF from the expected values.

Once enabled, the designed filter in question consists of

- two zeros at 15 Hz;
- two poles at 150 Hz.

and the magnitude and phase deviation from the expected is measured to be <0.5dB and <1deg below 10kHz.

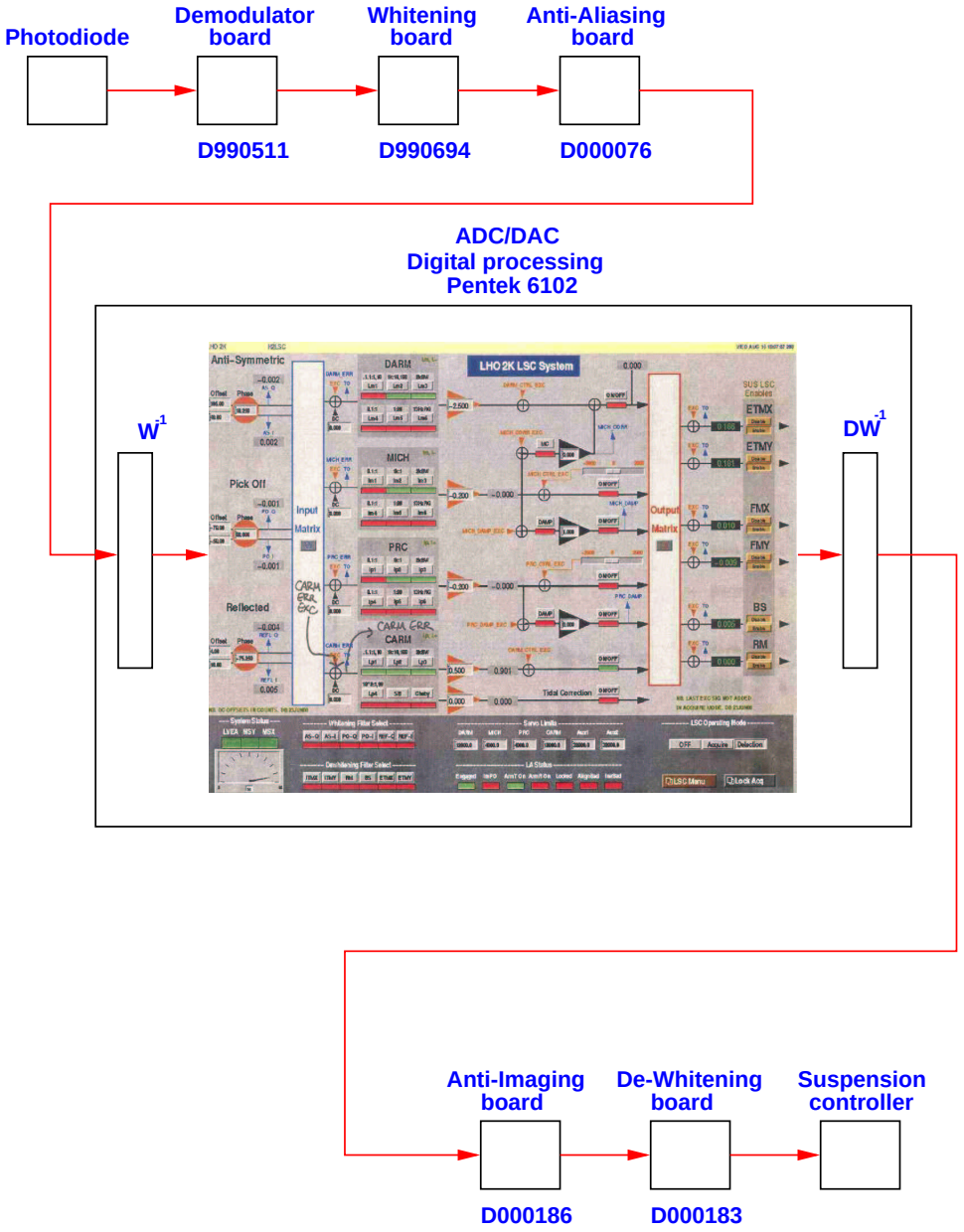

Figure 2: Signal processing: from PD to the LOS controllers.

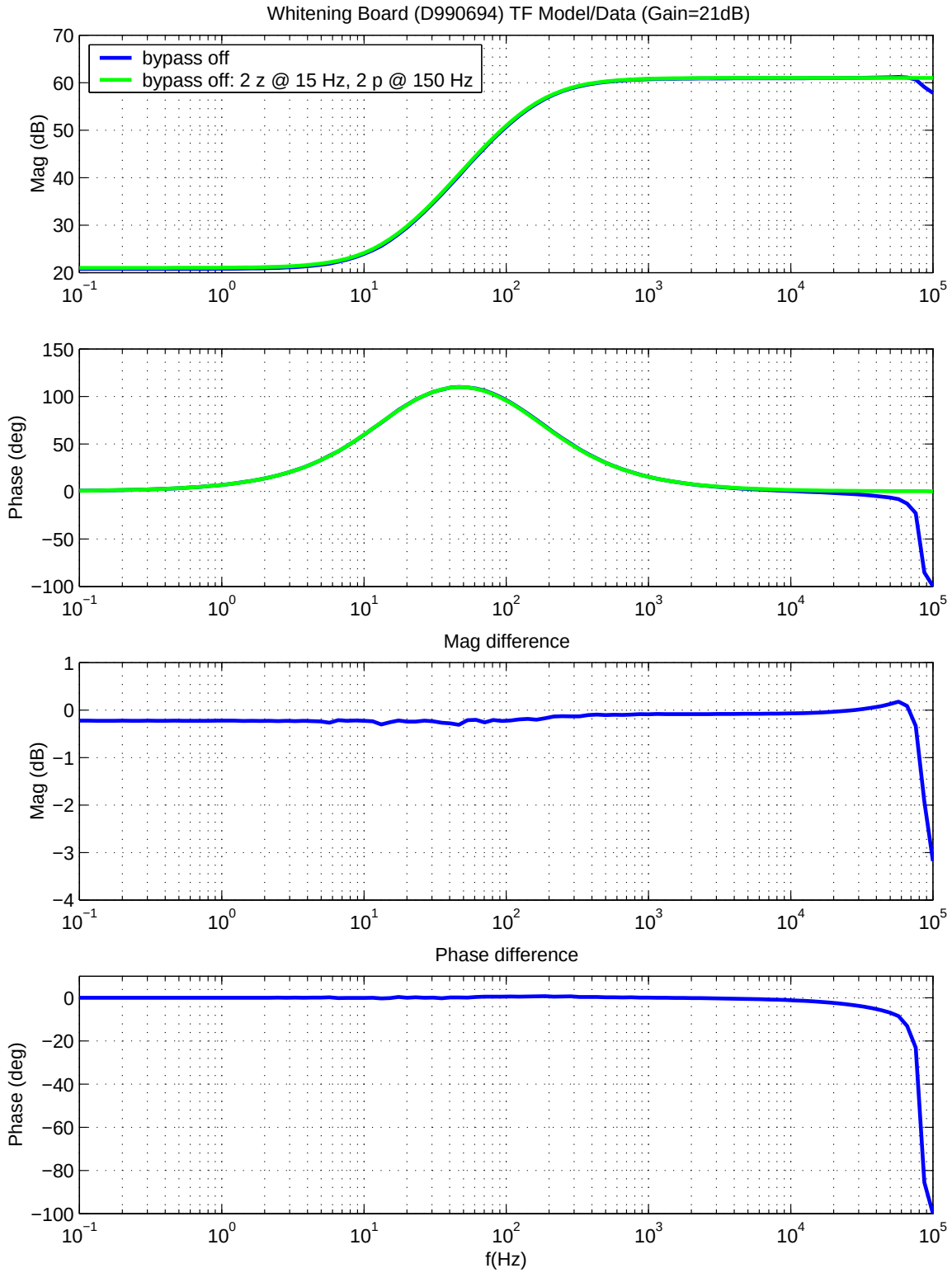

Figure 3: The TF of the Whitening filter.

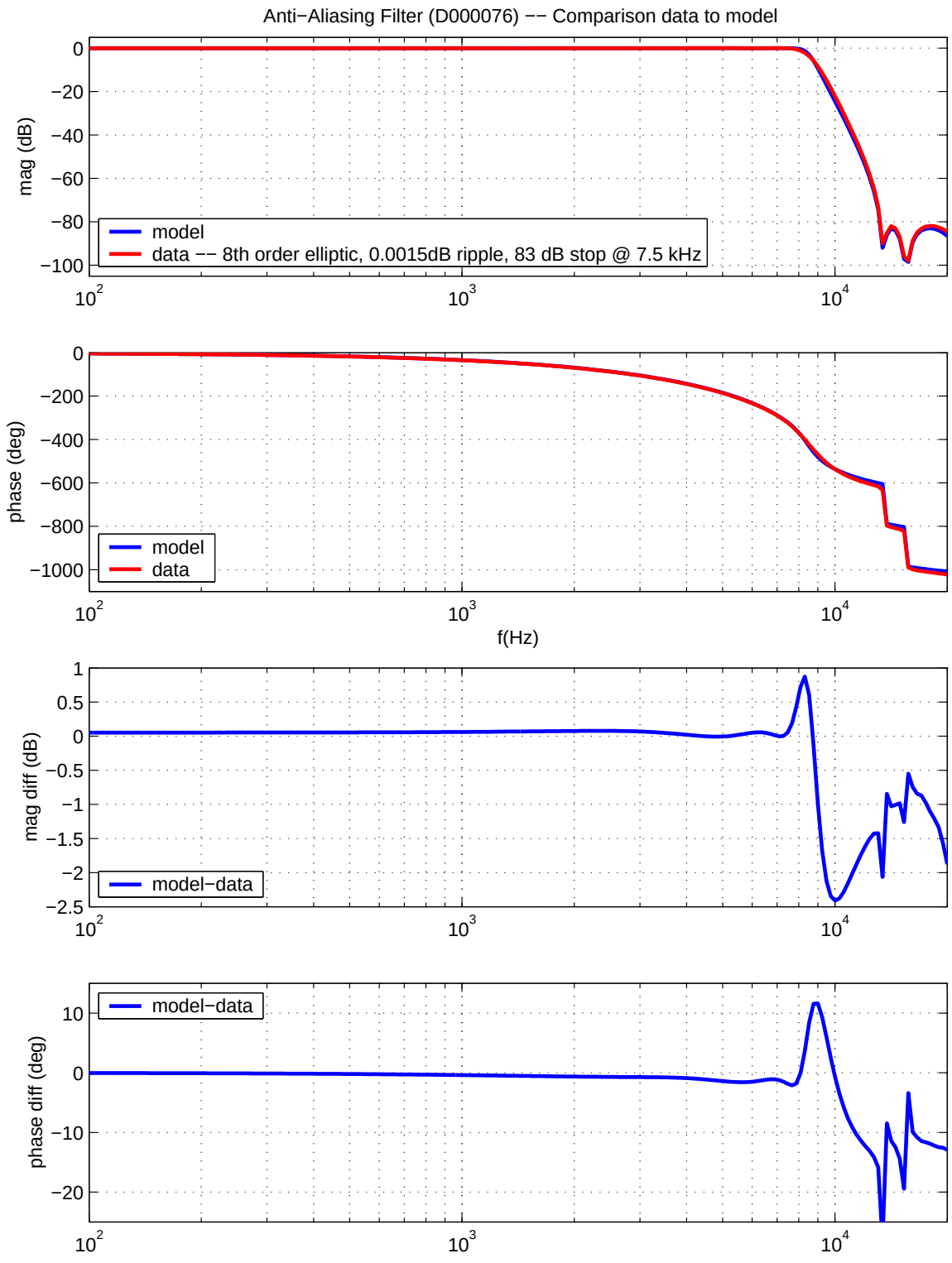

Figure 4: The TF of the Anti-Aliasing filter.

4.2 The Anti-Aliasing Board (D000076)

Fig.(4) shows the measured TF of the Anti-Aliasing board and compares it to an 8th order elliptic filter, whose ripple, attenuation and cutoff frequencies have been slightly adjusted from the designed parameters. The agreement is within 1dB and 2deg below 8kHz.

4.3 The Anti-Imaging Board (D000186)

Fig.(5) shows the comparison between the measured TF and a 4th order low-pass elliptic filter. Rev.A and Rev.B are both in use: the former is present in the mid-stations and consists of a 4th order elliptic filter whereas the latter is located in the LVEA and is a modified version of a 4th order elliptic filter. For rev.A, the agreement is within the 1dB level and 3 deg.

4.4 The De-Whitening Board (D000183)

Not measured. The digital bank of filters to revert the process of the board are called *dewhite* 1, 2, 3, 4 and are the inverse of the TF described on the schematics D000183.

4.5 The Digital Filtering

The bank of digital filters used to lock the complete IFO is here described. These filters are:

- .1.1:1,10
$$\frac{(s+2\pi 1Hz)\,(s+2\pi 10Hz)}{(s+2\pi 0.1Hz)^2} \tag{1}$$
- 1k:10,100
$$1000 \times \frac{(s+2\pi 10Hz)\,(s+2\pi 100Hz)}{(s+2000Hz(1+i)/\sqrt{(}2))(s+2000Hz(1-i)/\sqrt{(}2))} \tag{2}$$
- 2kBW
$$\frac{(2\pi 2000Hz)^2}{(s+2000Hz(1+i)/\sqrt{(}2))(s+2000Hz(1-i)/\sqrt{(}2))} \tag{3}$$
- 0.1:1
$$10 \times \frac{(s+2\pi 10Hz)}{(s+2\pi 0.1Hz)} \tag{4}$$
- 1:20
$$\frac{(s+2\pi 20Hz)}{(s+2\pi 1Hz)} \tag{5}$$
- 13HzRG
$$\frac{2\pi 12.4123Hz \times s}{s^2+2\pi 12.4123/20s+(2\pi 12.4123Hz)^2}+1 \tag{6}$$
- 1k:1
$$\frac{(2\pi 2000Hz)^2}{2\pi 1Hz}\,\frac{s+2\pi 1Hz}{(s+1000Hz(1+i)/\sqrt{(}2))(s+1000Hz(1-i)/\sqrt{(}2))} \tag{7}$$

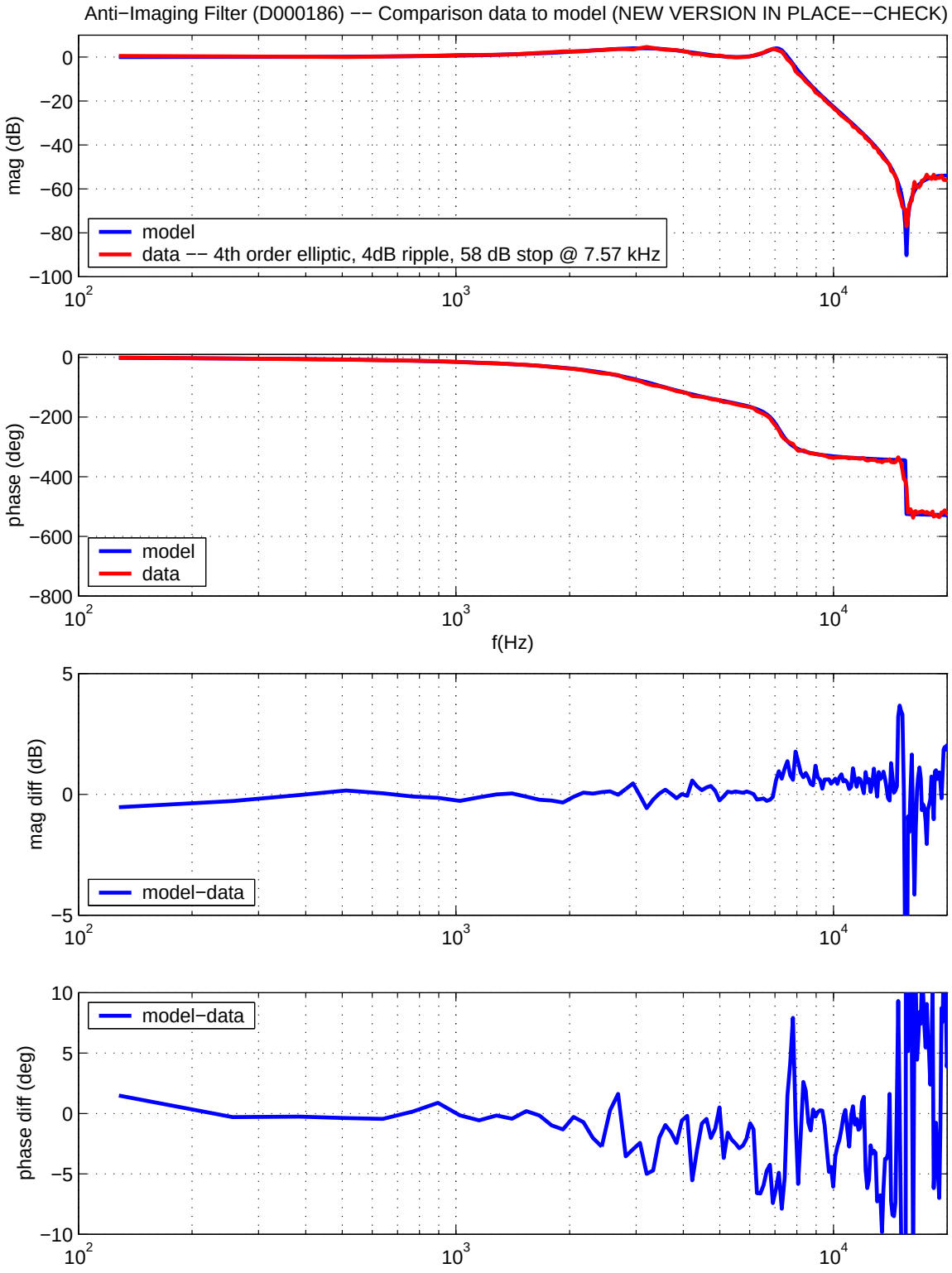

Figure 5: The TF of the Anti-Imaging filter.

- $\underline{10^2 : 1, 99}$

$$\frac{(s + 2\pi 1Hz)(s + 2\pi 100Hz)}{(s + 2\pi 10Hz)^2} \tag{8}$$

5 Delay Estimate

The TF from the Whitening to the Anti-Imaging board was measured with different digital filters enabled. By comparing the measurements to a Matlab model, we were able to give an estimate on the delay due to the ADC/DAC process. This was done by introducing a delay in the model that would fit the measured phase. Fig.(6) shows the result of one comparison. The top two graphs show the magnitude and phase of the measured TF (in blue) with the 2kBW filter enabled. The magnitude and phase produced by the model are shown in red. The green line is the TF phase of the model with an added delay of $75\mu s$. The bottom two graphs show the difference in magnitude and phase between the model and the measurements. Good agreement is achieved up to 8kHz.

For the purpose of this work, we will assume a speed of light of $2\times10^8 m/s$ in the fiber optic cable. This gives rise to a delay due to the light travel time to the mid-station of $2000m/(2 \times 10^8 m/s) = 10\mu s$.

6 The Mirror Actuator

The sections described above give an understanding of the filtering properties and delays in the LSC electronics. Now, we'd like to investigate the mirror actuators' frequency response.

To do this, we locked the 2k simple Michelson at LHO with FMX: the use of a relatively simple optical configuration simplified the analysis for the estimate of the actuators. The loop's gain was such that the Michelson was locked with a $10Hz$ bandwidth. Referring to the block diagram shown in Fig.(7), where

- C is the TF relating the (free) Michelson displacement $\delta l'$ to the demodulated signal (analog);
- W is the Whitening filter TF;
- AA refers to the Anti-Aliasing board;
- H includes the ADC/DAC processes, the different digital filters enabled and the computation delay;
- AI is the Anti-Imaging filter;
- DW represents the De-Whitening filter;
- Ax and Ay represent the actuators for FMX and FMY respectively
- δl is the Michelson's free running displacement noise and $\delta l'$ is the suppressed displacement noise;

we can express the TF between the error signal (after the ADC process) and the FMY excitation as

$$\frac{e}{y} = -\frac{1}{1 + C \times W \times AA \times H \times AI \times DW \times Ax} \times C \times W \times AA \times Ay \tag{9}$$

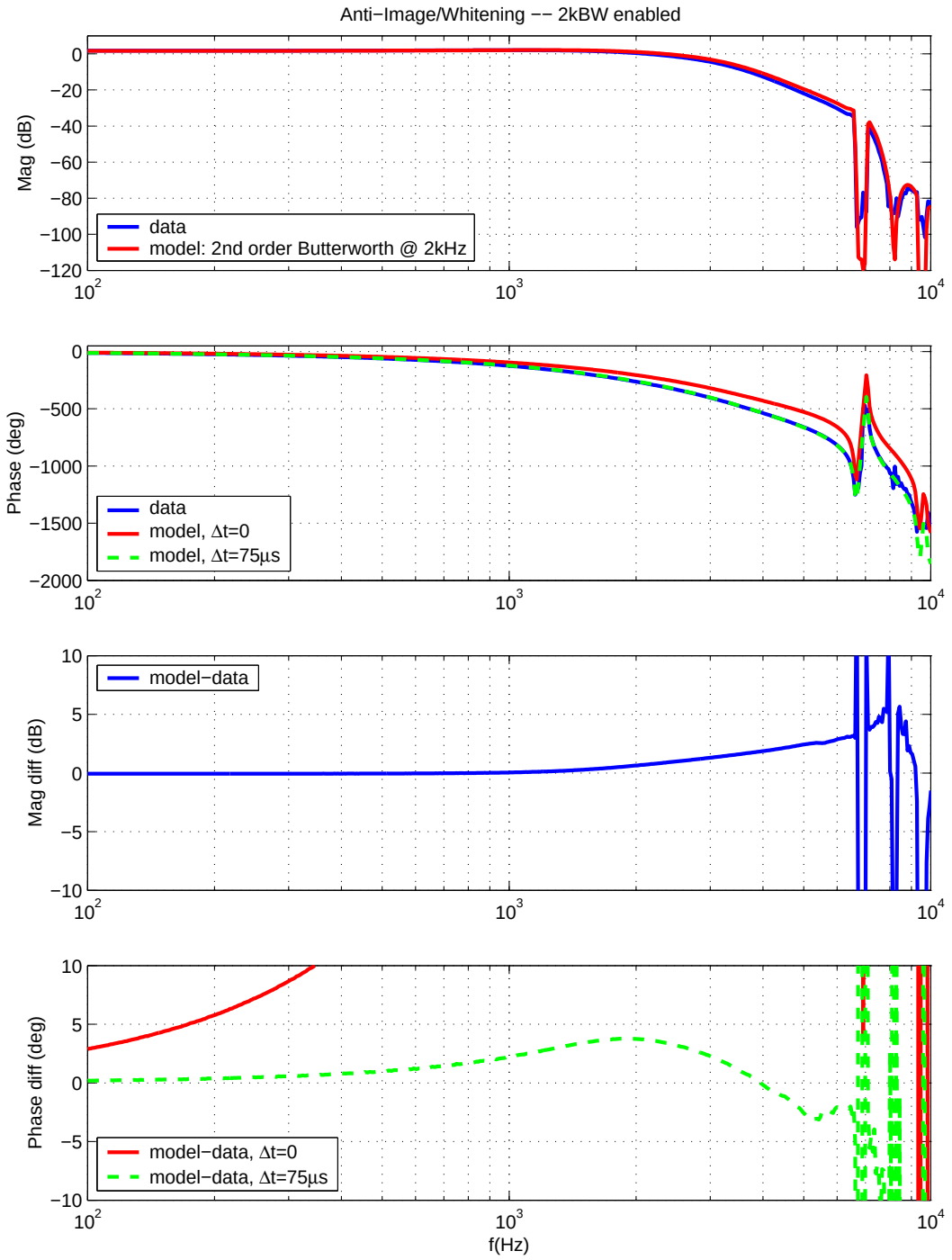

Figure 6: The TF from the Whitening to the Anti-Imaging board with the 2kBW digital filter enabled. Top two graphs: magnitude and phase of the transfer function (blue: measurement, red: model, green: model with delay). Bottom two graphs: difference between the measurement and the model in magnitude and phase.

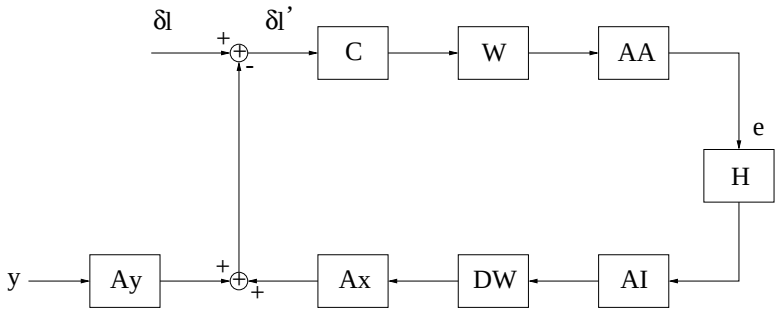

Figure 7: The block diagram for the actuator measurement.

If the measurement is carried out away from the UGF, eq.(9) can be reduced to

$$\frac{e}{y} = -C \times W \times AA \times Ay \tag{10}$$

measuring, therefore, the Anti-Aliasing and AY TF.

Fig.(8) shows two TF measurements between the error signal and the FMY excitation. The data represented in blue has a higher degree of coherence (at high frequency) than the green. The result of the model is also given. No parameters were adjusted nor added to improve the agreement, only a common gain factor was added. The TF magnitude is consistent to the expected $1/f^2$ roll off of the pendulum. The phase lead and lag shown in the measurements is also consistent with the model: the phase lead is caused by the closed loop TF with the UGF at 10Hz, whereas the phase lag is caused by the Anti-Aliasing board and the computation delay.

7 Accounting for the Phase in the Arms and Conclusions

In the previous sections, we described different aspects of the LSC. A Matlab model was then created based on the measured electronic TF and pendulum like frequency response for the mirror actuators. The accounting of the phase in the closed loop TF measurements for each arm is now addressed.

Fig.(9) and Fig.(11) show the measured closed loop TF for the X and Y arms respectively. The digital filters used in both cases are:

- .1.1:1,10
- 1k:10,100
- 2kBW

The results from the model is also shown, where only a common gain was adjusted to fit the data. The agreement between the expected and observed TF is in the 3dB and 10deg level.

The data shown in Fig.(9) and Fig.(11) is then used to estimate the open loop TF, shown in Fig.(10) and Fig.(12). The result of the model is also shown, giving a semi-quantitative (if not qualitative) understanding of the servo system.

The accord between the expected and the measured closed loop TFs grants us to use the model to investigate by how much each LSC component contributes to the total phase. Table (1) shows the model's results of such an investigation. As a result, the combination of the Anti-Aliasing and

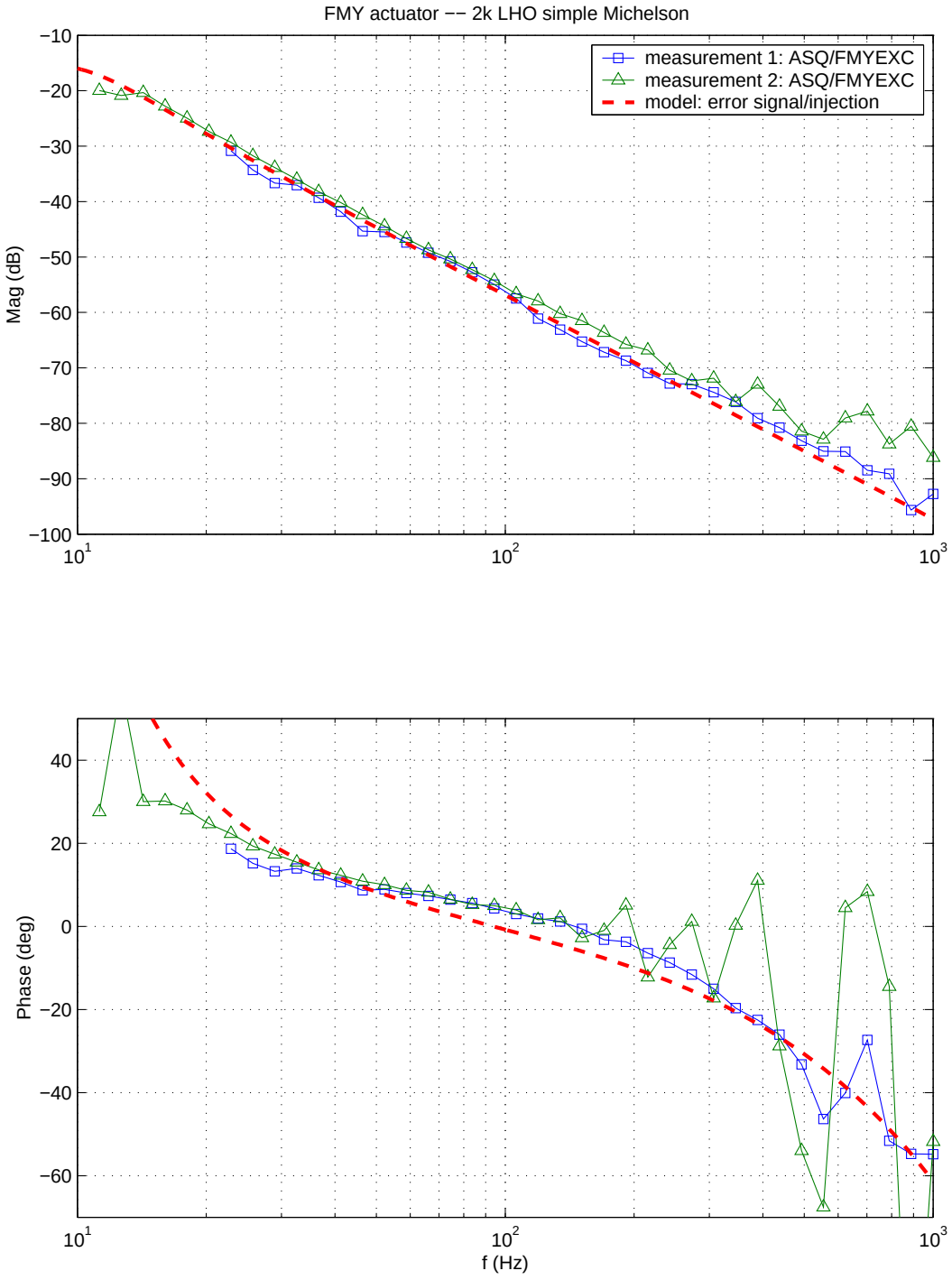

Figure 8: The TF between the error signal ASQ and the excitation signal FMYEXC. Two measurements were taken, the green one with more coherence at the 1kHz end. The expected TF, following eq.(9), is also shown.

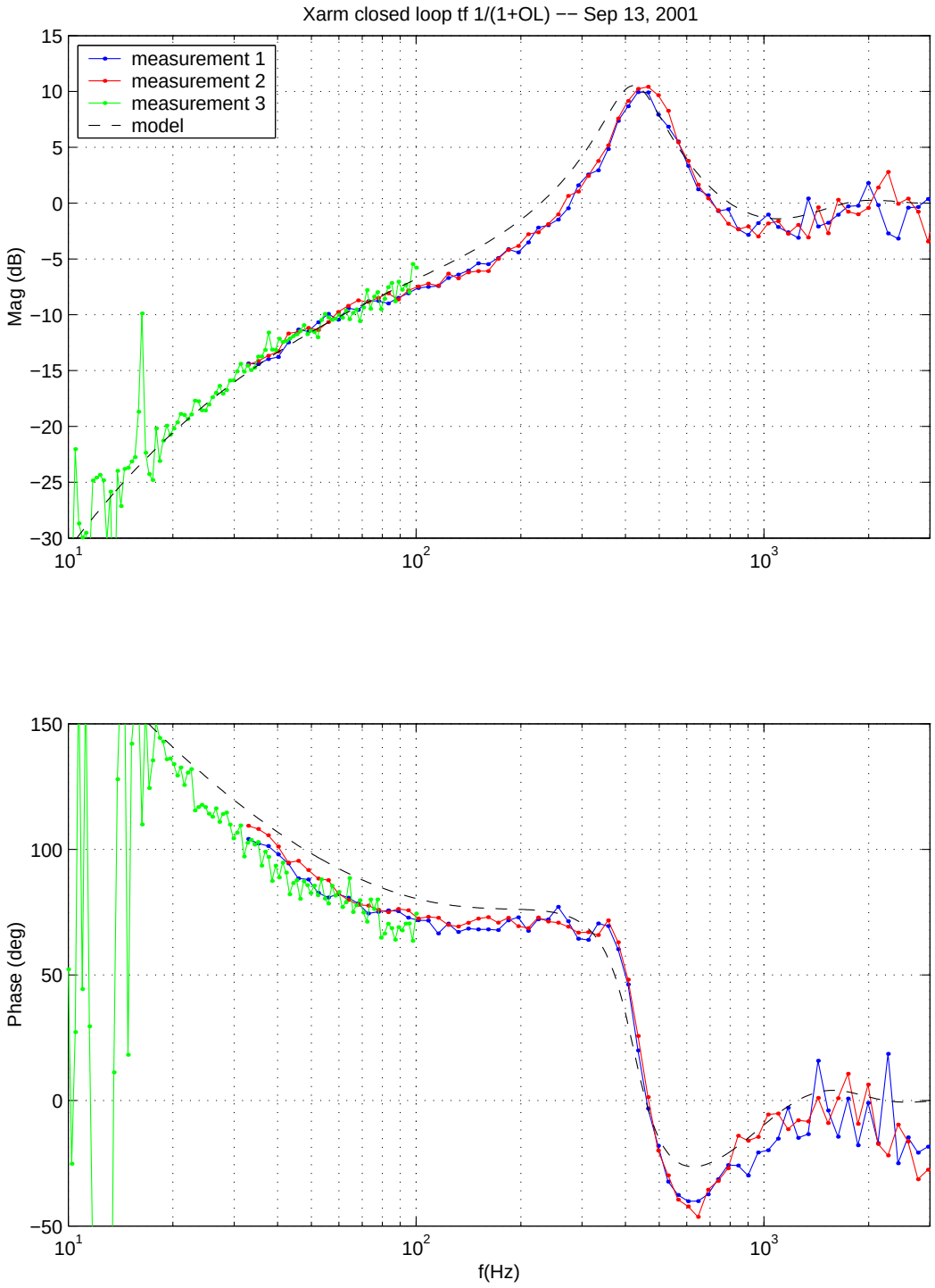

Figure 9: The closed loop TF for the X-arm: measurement/model.

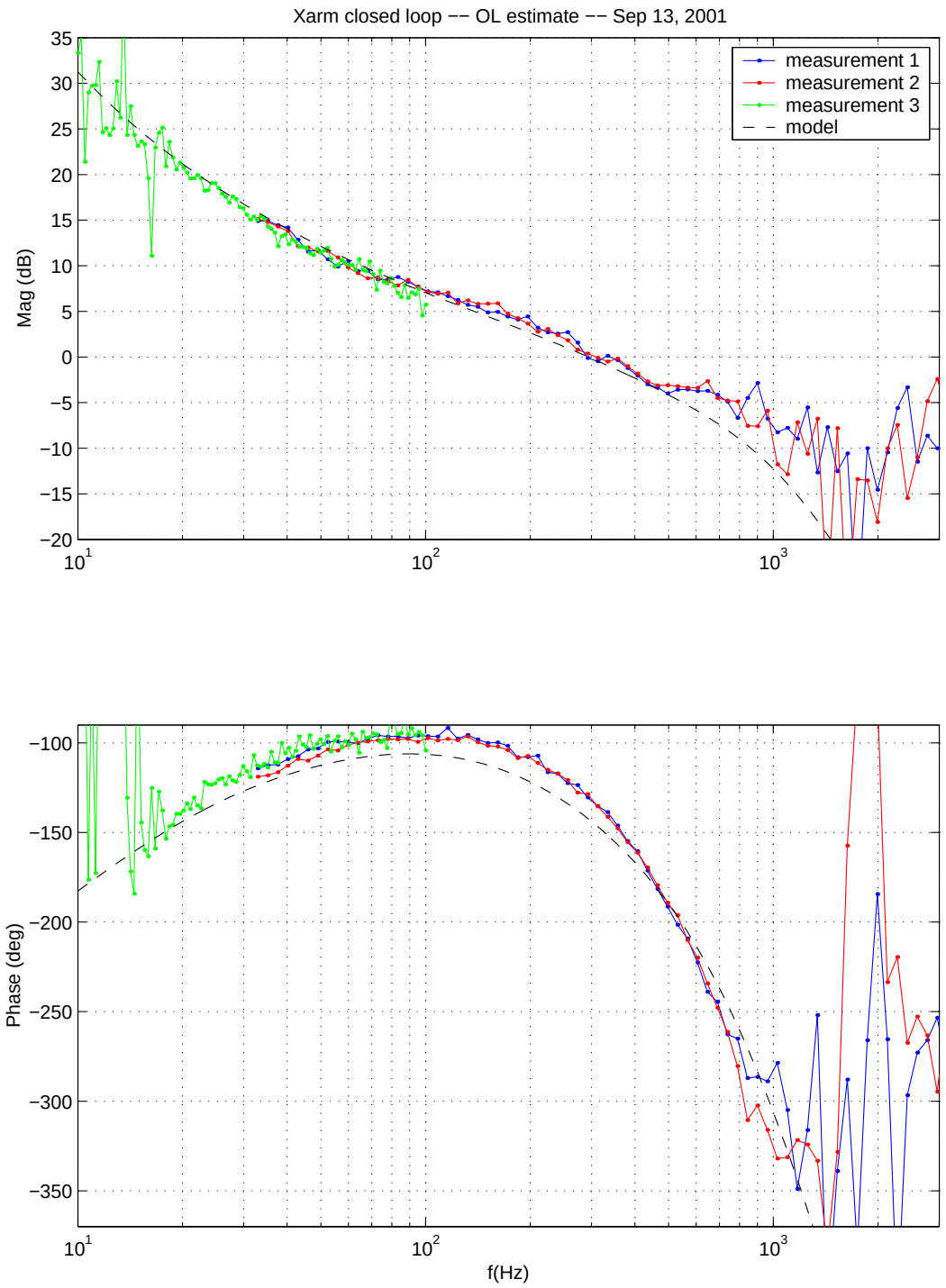

Figure 10: The open loop TF, in closed loop, for the X-arm: measurement/model.

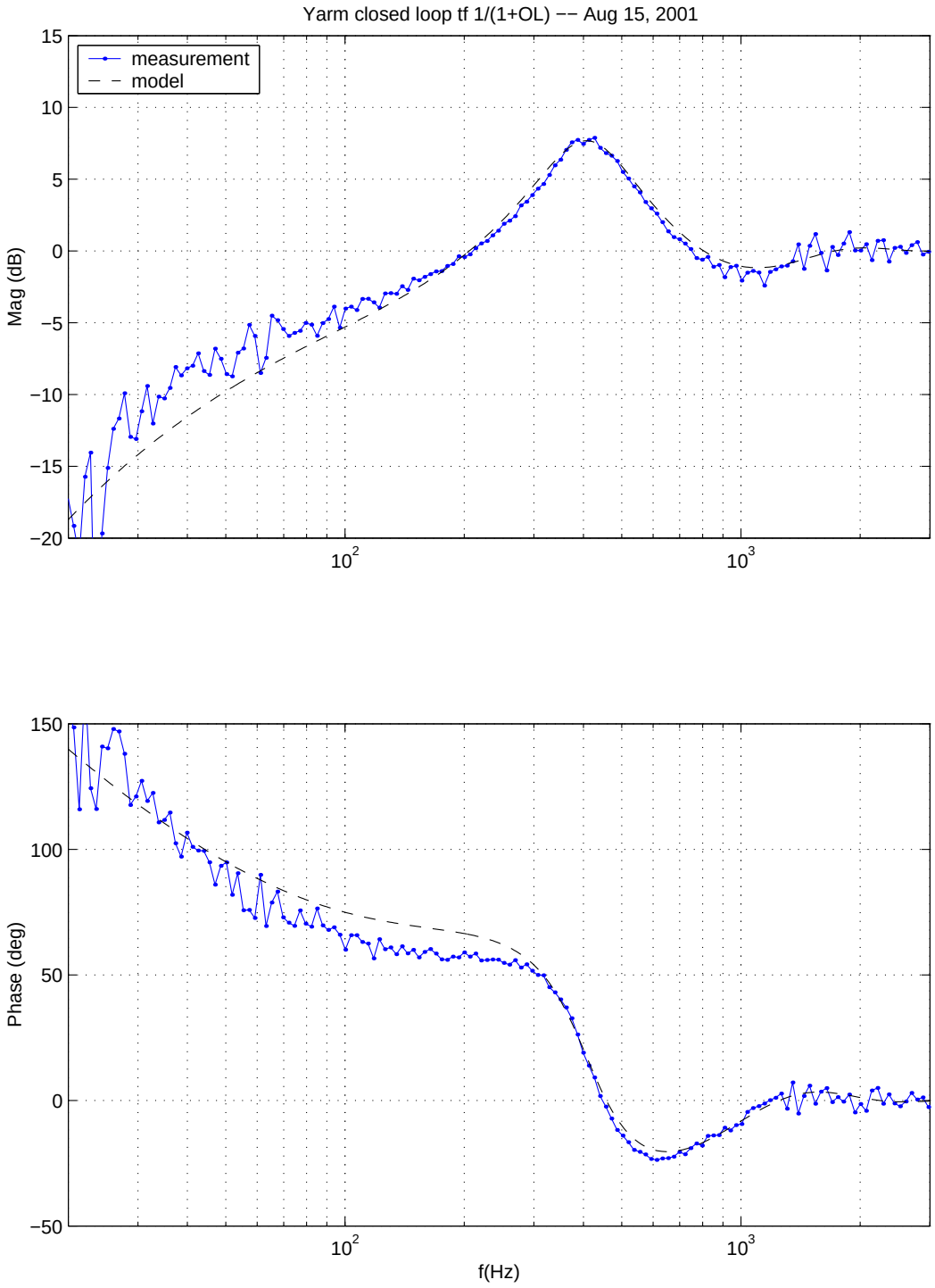

Figure 11: The closed loop TF for the Y-arm: measurement/model.

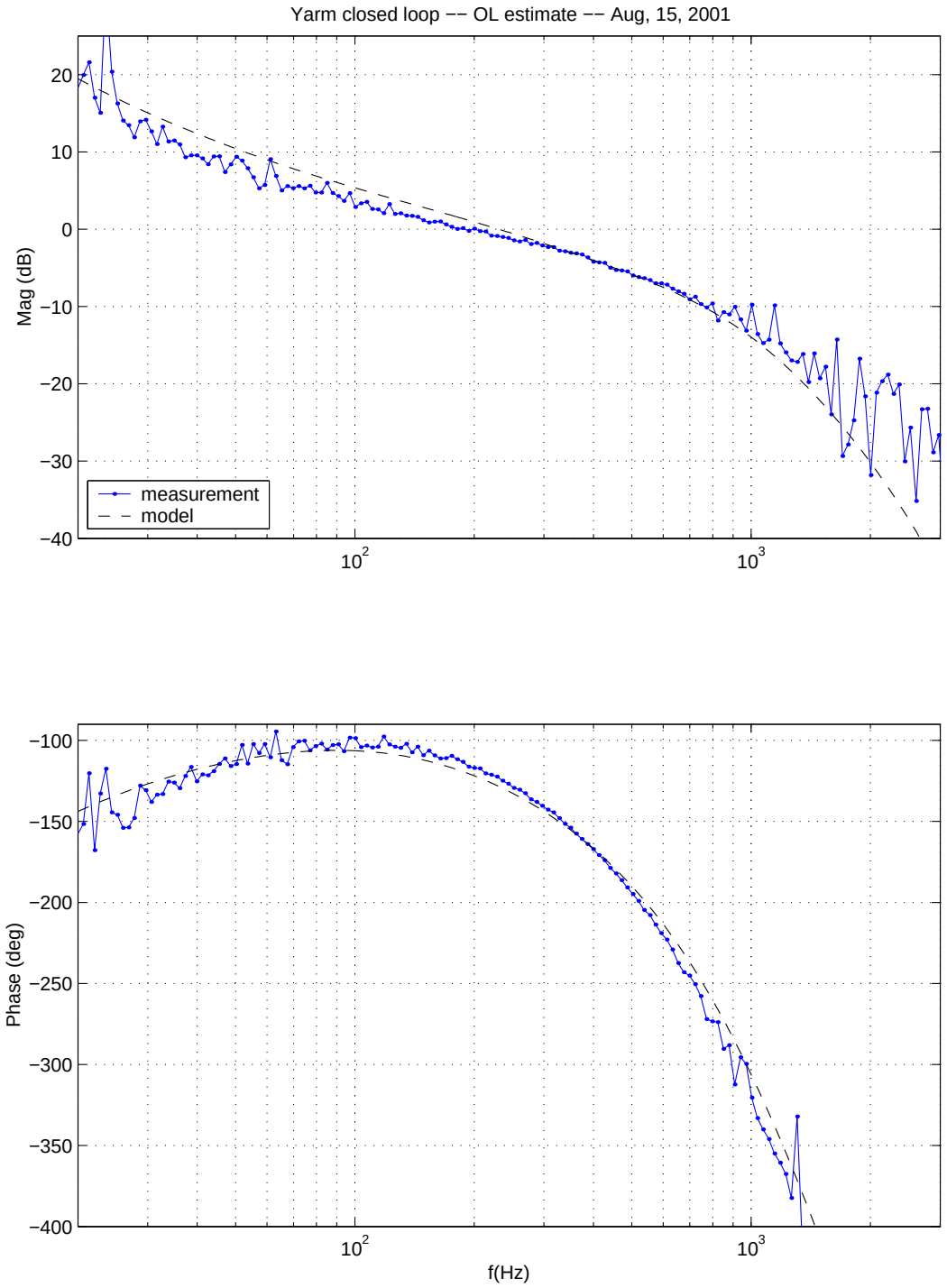

Figure 12: The open loop TF, measured in closed loop, for the Y-arm: measurement/model.

	$\delta\phi$ @ $100Hz$	$\delta\phi$ @ $500Hz$	$\delta\phi$ @ $1kHz$
s to z-domain	-2 deg	-10 deg	-15 deg
Anti-Imaging	-2 deg	-8 deg	-20 deg
Anti-Aliasing	-3 deg	-15 deg	-30 deg
Computation delay ($75\mu s$)	-3 deg	-14 deg	-30 deg
Round-trip travel time to mid ($2 \times 2km/210^8 m/s$)	-1 deg	-4 deg	-8 deg
Total	-11 deg	-51 deg	-103 deg

Table 1: The phase contribution $\delta\phi$ of each LSC component.

Anti-Imaging filtering, with the computation and travel time delays included and the s to z-domain process, gives rise to 50 deg at 500 Hz and 100 deg at 1kHz.

References

[1] LIGO-T980068-00-D "Length Sensing and Control Subsystem Final Design"

[2] LIGO-T970193-00-E "Overview of the End-to-End model"

[3] LIGO-T970084-00 "Frequency Response of the LIGO Interferometer"

[4] LIGO-T970122-00-D "Length Sensing and Control Subsystem Preliminary Design"

[5] LIGO-G980149-00-D "Interferometric Sensing and Control in LIGO"

[6] LIGO-P000008-A-D "Readout and control of a power-recycled interferometric gravitational wave antenna"

[7] R.W.P. Drever et al. "Laser phase and frequency stabilization using an optical resonator," Appl. Phy. **B31**, 97-105 (1983)